The landscape of myeloid and astrocyte phenotypes in acute multiple sclerosis lesions

Calvin Park[1], Gerald Ponath[1], Maya Levine-Ritterman[1], Edward Bull[1], Eric Swanson[2], Benjamin M. Segal[3], David Pitt[1]

[1] *Department of Neurology, Yale School of Medicine, New Haven, CT, USA*
[2]*Fluidigm Corporation, Markham, ON, Canada*
[3]*Department of Neurology, University of Michigan, Ann Arbor, MI, USA*

Author contact information
Calvin Park, Email: calvin.park@yale.edu
Gerald Ponath, Email: gerald.ponath@yale.edu
Maya Levine-Ritterman, Email: maya.levine-ritterman@yale.edu
Edward Bull, Email: embull@bowdoin.edu
Eric Swanson, Email: Eric.Swanson@fluidigm.com
Benjamin M. Segal, Email: bmsegal@med.umich.edu

Corresponding author
David Pitt, MD
Department of Neurology
Yale School of Medicine
300 George Street, Suite 353I
New Haven, CT 06511
david.pitt@yale.edu
Phone: 203-737-7951
Fax: 203-737-2704

Abstract

Activated myeloid cells and astrocytes are the predominant cell types in acute multiple sclerosis (MS) lesions. The polarization states of these cells play a critical role in lesion formation and resolution. To identify myeloid and astrocyte subsets present during lesion development, we profiled the cellular composition of an acutely demyelinating and an acute post-demyelinating MS lesion with thirteen immune markers, using imaging mass cytometry (IMC). In the early demyelinating lesion, distinct myeloid and astrocyte phenotypes populated separate lesion zones and engaged in specific interactions. In the late active lesion, phenotypes were less diverse and more uniformly distributed throughout the lesion. Our study demonstrates that multiplexed tissue imaging, combined with new computational tools, is a powerful approach to study cellular heterogeneity and spatial organization in MS lesions. Identifying glial phenotypes and their key interactions at different lesion stages may elucidate novel therapeutic targets for inhibiting acute demyelination and low-grade neuro-inflammation.

34 **Introduction**

35 Multiple sclerosis (MS) is a common neurological disease, characterized by formation of inflammatory demyelinating
36 lesions in the central nervous system (CNS) [21]. Inflammation is driven by infiltrating lymphocytes and monocytes,
37 in concert with resident activated microglia and astrocytes. Macrophages and reactive astrocytes are the most abundant
38 cell types in acute lesions [14,24]. These cells are highly plastic and can adopt pro-inflammatory, anti-inflammatory,
39 neurotoxic, neuroprotective, and tissue-regenerating functions [3,5,6,18,23,34].

40 Evaluating these cell phenotypes *in situ* is challenging. Previous studies have identified macrophage phenotypes in
41 MS lesions based on the expression of single classical (M1) and alternative (M2) activation markers; however, those
42 studies have produced limited and sometimes conflicting results [5,34]. Moreover, a recent study of traumatic brain
43 injury in mice demonstrated random expression of M1/M2 polarization markers in infiltrating macrophages in
44 seemingly incompatible combinations [12]. This suggests that the M1/M2 polarization paradigm, which originated as
45 an *in vitro* concept, is of limited value for characterizing myeloid cells in the inflamed CNS [28]. Instead, macrophages
46 within MS lesions exhibit complex phenotypes that cannot be captured by one, or several, M1/M2 markers, but instead
47 require high parameter evaluation.

48 Powerful new technologies, such as mass cytometry (CyTOF) and single cell RNA-sequencing, make it possible to
49 explore the heterogeneity of individual cell types. However, these methods do not capture the spatial information
50 contained in tissue, such as distribution and interactions of cellular subpopulations. This problem can now be
51 overcome with a novel imaging technology, imaging mass cytometry (IMC), which allows for quantitative profiling
52 with up to 37 antibodies on a single tissue section. Like CyTOF, IMC relies on metal isotope-labeled antibodies, and
53 combines immunohistochemistry with high-resolution laser ablation followed by time-of-flight mass spectrometry
54 [35]. In parallel, novel computational tools have become available to extract single-cell information from highly
55 multiplexed histological data.

56 We applied IMC and single-cell analytics to two active MS lesions – one acutely demyelinating and one active but
57 post-demyelinating – to examine the cellular heterogeneity of myeloid cells and astrocytes, based on thirteen immune
58 function markers. We demonstrate here that multiplexed tissue imaging, in combination with the appropriate
59 computational tools, can extract previously unattainable information on single cells from histological sections. This
60 includes cellular subpopulations and their distribution within the lesion environment, specific cell-cell interactions,

61 phenotypic transitions, and the impact of the lesion environment on marker expression. High-dimensional
62 characterization of MS lesions will ultimately provide a complete picture of polarization states, and of the nodal points
63 of cellular communication that are critical for lesion formation, chronic low-grade inflammation, and lesion resolution.

64

65 **Results**

66 *Histology and cell clustering overview*

67 We analyzed one actively demyelinating and one active post-demyelinating MS lesion, according to a classification
68 by Kuhlmann et al. [13], referred to throughout this report as the "early" and "late" lesion, respectively. Both lesions
69 were located in the brain stem and characterized by complete loss of myelin, hypercellularity with the highest cellular
70 density at the lesion rim, and diffuse infiltration with foamy macrophages. The laser-scanned area of the early lesion
71 involved predominantly white matter (WM) but also interspersed gray matter (G/WM), while the scanned area of the
72 late lesion consisted of only WM (Figure 1).

73 Consistent with demyelinating activity, macrophages at the rim of the early lesion contained myelin basic protein
74 (MBP)-positive myelin debris, which was absent in macrophages from the late lesion (Figure 1d, j) [13]. Moreover,
75 foamy macrophages were numerous and large in size in the rim of the early lesion, whereas macrophages in the
76 rim of the late lesion were smaller and less concentrated (Figure 1e, k).

77 Perivascular infiltrates in the early lesion contained mostly lymphocytes and only a few undifferentiated monocytes,
78 while the perivascular cuffs in the late lesion consisted predominantly of lipid-laden macrophages, as described
79 previously (Figure 1i, l) [17,32]. We defined single cells by segmenting cell bodies outlined by the markers CD68
80 (macrophages/microglia), S100B (astrocytes), and CD3 (T cells) using CellProfiler (Figure 2) [11]. This allowed for
81 a clear delineation of cell types in the vast majority of cells. In a small fraction of cells, we found overlap between
82 cellular markers, especially between myelin fibers and juxtaposed microglial processes in normal-appearing white
83 matter (NAWM), and between astrocyte processes and closely neighboring macrophages (Figure 2c, d). We did not
84 exclude these cells in order to avoid bias in our spatial analysis. However, we excluded perivascular lymphocytes
85 from the early lesion, as they were too densely packed to be identifiable as individual cells.

86 Segmentation masks were overlaid with corresponding images from thirteen antibody channels (Figure 3—figure
87 supplement 1; Figure 5—figure supplement 1) in histoCAT [29], which clustered myeloid cells and astrocytes into
88 phenotypic subpopulations based on their marker expression profiles. The optimal number of phenotype clusters was
89 determined based on separation of the principal cell types (i.e. myeloid cells, astrocytes and T cells) and distinctive
90 expression profiles of phenotypes, using expression heatmaps and t-SNE plots. With twelve phenotypes per lesion,
91 we demonstrated that the main cell types and their subpopulations separated into distinct clusters (Figures 3, 5).

92 *Phenotype heterogeneity and distribution in early demyelination*

93 In the early lesion, we analyzed a total of 4,397 cells, of which 66.3% were myeloid cells and 32.5% were astrocytes
94 (Figure 3—figure supplement 2a). This ratio was higher at the rim than the lesion center. The cells clustered into six
95 myeloid and five astrocyte subtypes (Figure 3). The myeloid phenotypes were spatially sequestered in four lesional
96 regions, i.e. NAWM, outer lesion rim, inner lesion rim, and center. Within the outer lesion rim, we observed one
97 myeloid cell phenotype at the G/WM interface (m1) and two phenotypes located in the WM rim (m4, m5). The other
98 lesion areas were all occupied by one myeloid phenotype (Figure 4a). Most myeloid cell activation markers were
99 highly expressed in the outer lesion rim and decreased in intensity towards the lesion center (Figure 3a, b). The m1
100 phenotype at the G/WM interface showed the highest activation profile. m5 cells in the outer WM rim were the largest
101 in size, whereas m2 cells in the lesion center were the smallest (Figure 3—figure supplement 2b); this may reflect the
102 amount of myelin fragments phagocytosed by foamy macrophages at the advancing lesion edge, and the degradation
103 of myelin in phagocytes within the lesion center [25].

104 Astrocyte phenotypes were each defined by one distinct, highly expressed marker (Figure 3a, b). Analogous to the
105 myeloid phenotypes, the five astrocyte phenotypes were also spatially stratified into the NAWM, lesion rim, and lesion
106 center (Figure 4b). Furthermore, a5 astrocytes located in the outer rim within WM were larger than all other
107 phenotypes (Figure 3—figure supplement 2b). Unlike in myeloid cells, marker expression in astrocytes did not follow
108 a gradient from the rim to the lesion center, but was uniform throughout the lesion.

109 T cells made up the smallest population of all immune infiltrates, and were concentrated within the lesion center
110 (Figure 4c; Figure 3—figure supplement 2a). These cells uniformly expressed CD45 and HLA-DR (Figure 3a, b), and
111 did not separate into different clusters.

112 To determine possible transitions between phenotypes, we applied Potential of Heat-diffusion Affinity-based
113 Transition Embedding (PHATE) mapping and Pseudotime to the myeloid cell and astrocyte populations. PHATE
114 mapping improves on t-SNE by better visualizing phenotype transitions, where smooth continua from one phenotype
115 to another indicate a transition trajectory [19]. Rather than a rim-to-center continuum that aligned with the sequential
116 organization of phenotypes in the lesion, our analysis showed only a partial continuum between the G/WM outer rim
117 phenotype (m1) and the lesion center phenotype (m2) (Figure 4d), without including the inner rim phenotype (m3).
118 Similarly, analysis with Pseudotime, an alternative tool for visualizing phenotype transitions [33], showed that
119 myeloid phenotypes did not follow a linear transition trajectory but branched into several independent fates (Figure
120 4e). PHATE mapping and Pseudotime analysis of astrocyte phenotypes also suggested independent phenotypic fates
121 rather than linear phenotype trajectories (Figure 4—figure supplement 1, Pseudotime analysis not shown).

122 *Low phenotype heterogeneity and random phenotype distributions in the late demyelinating lesion*

123 In the late, post-demyelinating lesion we analyzed 6,698 cells, with myeloid cells far outnumbering astrocytes (91.1%
124 myeloid cells; Figure 5—figure supplement 2a), particularly at the lesion rim. The same clustering criteria used for
125 the early lesion resulted in nine myeloid phenotypes and two astrocyte phenotypes in this late lesion (Figure 5).
126 Myeloid phenotypes separated into lesion rim (m3), perivascular space (m4), and NAWM (m7) zones (Figure 6a). In
127 contrast to the early lesion, the other six myeloid phenotypes were intermixed throughout the lesion center. These
128 phenotypes showed a low degree of separation on the t-SNE plot, indicating similar marker expression profiles (Figure
129 5c). The phenotypes in the lesion rim and the perivascular space (m3, m4) were characterized by high expression of
130 the majority of markers, and shared a similar expression profile with the G/WM rim phenotype in the early lesion
131 (m1) (Figure 5a, b). Other myeloid subpopulations did not overlap between the two lesions. Phenotypes in the lesion
132 rim (m3) and perivascular space (m4) were significantly larger than the lesion center phenotypes (Figure 5—figure
133 supplement 2b). Overall, myeloid cells were significantly smaller in the late lesion than in the early lesion (data not
134 shown).

135 Astrocytes were clustered into two phenotypes, with one phenotype localizing primarily to the lesion rim, and the
136 other to the lesion center (Figure 6b). The rim phenotype (a2) exhibited a marker expression profile similar to the rim
137 phenotype in the early lesion (a5), while the lesion center phenotype did not overlap with any astrocyte phenotypes in

138 the early lesion (Figure 5a, b). Finally, T cells were few (Figure 6c; Figure 5—figure supplement 2a), and expressed
139 the activation markers CD45 and HLA-DR (Figure 5a, b), as observed in the early lesion.

140 PHATE mapping demonstrated a partial continuum between two lesion center myeloid phenotypes (m2, m6) and the
141 perivascular space phenotype (m4) (Figure 6d), which was confirmed by Pseudotime (Figure 6e). These analyses
142 support a lesion center-to-perivascular transition, but not a continuum where all phenotypes align along a rim-to-center
143 transition axis. The same analyses for astrocytes showed substantial overlap between both phenotypes but not a linear
144 transition (Figure 6—figure supplement 1, Pseudotime analysis not shown).

145 In the early lesion, we found no correlation between the expression intensities of different markers at a single-cell
146 level (Figure 7—figure supplement 1a, b). This was true for an analysis of all cells and cells of each phenotype (data
147 not shown). In the late lesion, we found strong correlations between the M2 markers MerTK and Mac2, and MerTK
148 and LAMP1 in both myeloid cells and astrocytes (Figure 7—figure supplement 1c, d). This resulted from high and
149 continuous dynamic ranges of marker expression (Figure 7). Correlations were weak between the other marker pairs.

150 *Phenotypes in the early and late acute lesions engaged in specific cell-cell interactions*

151 We next investigated the spatial relationships between different phenotypes with a computational tool integrated into
152 histoCAT that performs an unbiased, systematic analysis of pairwise phenotype interactions and avoidances [29].
153 After excluding interactions between cells of the same or spatially adjacent phenotypes, our analysis demonstrated
154 distinct interaction signatures for both lesions, (Figure 8a, b). At a significance cut-off of $p < 0.01$, these included
155 interactions between inner rim myeloid phenotype m3 (MerTK and CD45 high) and astrocyte phenotype a1 (Mac2
156 high), as well as interaction of highly activated myeloid rim phenotype m1 and the rim/center phenotype m4 (HLA-
157 DR and ferritin high) with astrocyte phenotype a2 (HLA-DR high) in the early lesion. In the late lesion, highly
158 activated perivascular macrophages (m4) interacted with most myeloid cell phenotypes and both astrocyte phenotypes.
159 There were also significant interactions between myeloid and astrocyte phenotypes m6 and a1, and among lesion
160 center myeloid phenotypes (m6 with m7 and m8). At a significance cut-off of $p < 0.05$, we found that T cells in the
161 late lesion interacted with myeloid phenotypes in the perivascular space (m4), which expressed HLA-DR, and in the
162 lesion center (m8).

163 *Influence of lesion environment on marker expression*

164 Finally, we used spatial variance component analysis (SVCA) to model the effects of extrinsic factors (neighboring
165 cells and non-cellular environmental stimuli) and cell-intrinsic factors on variations in cell marker expression [2]. In
166 the rim of both lesions, the expression of several markers was highly influenced by neighboring cells, including CD86,
167 PLP, and Mac2 in the early lesion, and CD86, PLP and LAMP1 in the late lesion. Other markers, such as ferritin,
168 vimentin, and CD3 (early lesion), and ferritin, vimentin, and TIM-3 (late lesion), were driven predominantly by non-
169 cellular environmental stimuli (Figure 8c, d). The relative influence of these factors changed toward the inner lesion
170 rim and center, leading to an overall increased impact of cell-intrinsic factors and a decrease in the influence of external
171 factors. In the lesion center, the primary agents influencing marker expression were cell-intrinsic factors and, to a
172 lower degree, environmental stimuli (Figure 8c, d).

173

174 **Discussion**

175 Our study examines the landscape of myeloid and astrocyte phenotypes in early and late acute MS brain lesions using
176 imaging mass cytometry. To our knowledge, this is the first application of highly multiplexed imaging to MS lesions.
177 We applied thirteen glia-related markers to MS lesions, which clustered myeloid cells and astrocytes into eleven
178 phenotypes. The phenotypes localized to different lesional zones, suggesting functional specificity. We further
179 characterized specific spatial interactions between phenotypes, examined phenotypic transitions within lesions and
180 determined the effect of cell-extrinsic and -intrinsic factors on marker expression in individual cells. Thus, our study
181 demonstrates that highly multiplexed imaging, combined with computational tools, provides a wealth of data on
182 cellular spatial organization that is not accessible with standard histology.

183 Our findings contrast with recent attempts to cluster myeloid cells in experimental autoimmune encephalomyelitis
184 (EAE), a mouse model of MS, with single-cell cytometry [20], and in white matter MS lesions with RNA-sequencing
185 data [10], which resulted in only two myeloid cell subpopulations, respectively. The higher number of clusters in our
186 study might be explained by the targeted set of markers, which are relevant to glial biology. In contrast, RNA-
187 sequencing emphasizes highly expressed genes, and might not detect low-expression genes or subtle differences in
188 gene expression that may be important for glial phenotype clustering.

189 We found that the myeloid cell phenotypes separated into different layers within the lesion, including the NAWM,
190 outer and inner lesion rims located in the WM or mixed G/WM matter, and the lesion center. This alignment of

191 phenotypes with lesional zones confirms the validity of our clustering approach. Consistent with the different stages
192 of myelin phagocytosis and degradation, the phenotypes in the rim and lesion center displayed different cellular sizes.
193 Only one myeloid phenotype was shared by both lesions, located in the lesion rim (m1 in the early lesion; m3 in the
194 late lesion), while all other phenotypes were unique to their respective lesions. Phenotypes were distinctly stratified
195 in the early demyelinating lesion, while their distribution in the post-demyelinated lesion appeared less ordered,
196 especially in the lesion center. Moreover, expression of all activation markers, with the exception of CD68, was high
197 in myeloid cells at the lesion rim and diminished substantially toward the lesion center. While the rim-to-center
198 gradient also existed in the late lesion, it was less pronounced. Thus, whereas the high activation profile of myeloid
199 cells at the lesion rim remained consistent between the two lesions, the center phenotypes lost their location-specific
200 polarization in the late lesion and became functionally less distinct. An additional feature of the late lesion was highly
201 activated macrophages that populated perivascular spaces in large numbers throughout the lesion. Since these
202 macrophages are believed to exit the CNS [17], this indicates that macrophages leave the CNS in a highly activated
203 state. Marker expression in astrocytes did not follow a rim-to-center gradient, but remained comparable throughout
204 the lesion area in both lesions.

205 Our findings argue that macrophages/microglia in MS lesions do not transition from a pro- to anti-inflammatory state,
206 as previously suggested [5], but convert from a highly activated to a less activated state as they move from the active
207 edge to the lesion center. This is consistent with a study by Vogel and colleagues, who demonstrated that pro- and
208 anti-inflammatory markers were simultaneously expressed by macrophages/microglia in MS lesions [34]. Our results
209 therefore provide further evidence that activated macrophages in inflamed tissue do not follow a M1/M2 polarization
210 dichotomy [28]. However, clarification of this question requires functional assays and/or a more detailed evaluation
211 of pro-inflammatory and immunosuppressive pathways in these cells. Two recent reports, including our own, suggest
212 a dichotomy in MS and EAE between myeloid cells expressing inducible nitric oxide synthase (iNOS) or arginase,
213 two enzymes that both use the substrate L-arginine to generate either reactive nitric oxide species or substrates such
214 as urea and L-ornithine that contribute to tissue repair [7,16].

215 Using PHATE mapping and Pseudotime to determine transitions between phenotypes, we did not find that myeloid
216 cell or astrocyte phenotypes developed along a linear transition continuum, i.e. from the outer to the inner lesion rim
217 and lesion center. Instead, the different phenotypes branched into multiple independent trajectories, suggesting that
218 they emerge within the lesion environment independently from each other. We cannot exclude that the parametric

219 depth of our study is too low to detect transition states, especially since Pseudotime has been developed to delineate
220 phenotypic trajectories from whole transcriptome sequencing data [33]. Nevertheless, since clustering with our set of
221 markers resulted in lesion zone-specific phenotypes, it is conceivable that the same markers can be used to trace
222 transitions between the lesion phenotypes.

223 Neighborhood analysis demonstrated distinct cellular interaction signatures for both lesions, e.g. between phagocytic
224 macrophages in the inner rim and center astrocytes in the early lesion, and between T cells and myeloid phenotypes
225 in the late lesion. Thus, interactions in the hypercellular lesion environment are not random, but occur between specific
226 subpopulations and cell types such as lymphocytes. The low parametric depth of our study does not allow us to identify
227 the functional implications of these interactions; however, they may represent nodal points of cellular communication
228 that are key for lesion formation and maintenance of low-grade lesional inflammation.

229 Finally, spatial variance component analysis (SVCA) suggests that cell-extrinsic factors drive marker expression to a
230 higher degree at the rim than in the lesion center. Conversely, cell-intrinsic factors have a more prominent influence
231 on marker expression in the lesion center than at the rim. This indicates that glia cells in the lesion rim are more
232 responsive to cues from the microenvironment, such as cytokines or receptor-ligand interactions, while glia responses
233 in the lesion center are more affected by cell-intrinsic programs such as cellular changes that are set in motion by
234 myelin phagocytosis.

235 In summary, we found that phenotypic clustering, determined through differential expression of thirteen markers,
236 produced multiple myeloid cell and astrocyte phenotypes that occupied specific lesion zones in the early acute lesion,
237 and were more randomly distributed in the late lesion. Myeloid cells were activated along a rim-to-center axis, and
238 specific myeloid cell-astrocyte-lymphocyte interactions were present in both lesions. Thus, our study highlights the
239 potential of imaging mass cytometry and other highly multiplexed imaging techniques [4,8] to provide insight into
240 lesion-forming phenotypes and their spatial formation. In addition, our study provides novel insight into the dynamics
241 of phenotypes and their spatial organization in MS lesions over time.

242 The study is limited by the small sample size and the small number of markers, which does not allow for deep
243 functional characterization of phenotypes. In ongoing studies, we are combining clustering based on single nuclear
244 RNA-sequencing data of glial cells, derived from MS lesion tissue, with highly multiplexed imaging of the same
245 lesion, to simultaneously obtain maximal parametric depth and high spatial resolution at single-cell level. This will

246 eventually define the phenotypes and key interaction networks that drive active demyelination and chronic, low-grade
247 inflammation in established lesions and may provide targets for therapeutic intervention in relapsing and progressive
248 MS.

249

250 **Materials and methods**

251 ***MS lesions.***

252 Human CNS tissue was obtained at autopsy from two patients with relapsing-remitting MS according to Institutional
253 Review Board-approved protocols. After autopsy, brain tissue was fixed in 10% formalin, and lesions were cut based
254 on MRI. Lesion tissue was subsequently embedded in paraffin and sectioned at 5 µm thickness.

255 A highly inflamed, active lesion was chosen for analysis from each patient: the actively demyelinating lesion was
256 selected from a 42-year-old male with 5 years disease duration (5.5 hour *post mortem* interval), while the post-
257 demyelinating lesion was chosen from a 32-year-old female with 6 years disease duration (8 hour *post mortem*
258 interval). Lesions from both patients have been characterized in previous studies [7,22].

259 ***Brightfield histology.***

260 For basic characterization, lesions were stained against CD68, myelin basic protein (MBP) and neuronal marker
261 MAP2, and examined with brightfield microscopy. De-paraffinized and rehydrated sections were subjected to antigen
262 retrieval in pH 6, 10 mM citrate buffer at 96°C for 20 minutes, cooled, quenched in 0.3% peroxide, and blocked with
263 FC receptor binding inhibitor and normal serum before incubation with primary antibody (Table 1) overnight at 4°C.
264 Sections were subsequently incubated with appropriate biotinylated secondary antibodies, processed with an
265 avidin/biotin staining kit with 3,3-diaminobenzidene (DAB) as the chromogen (Vector ABC Elite Kit and DAB Kit,
266 Vector Laboratories, Burlingame, CA, USA), then counterstained with hematoxylin [22]. Adequate controls using
267 isotype control antibodies were performed for each primary antibody. Sections were rinsed with distilled water,
268 dehydrated, and cover-slipped with Permount (Vector Laboratories). Images were acquired using a Leica DM5000 B
269 microscope with a Leica color camera DFC310 Fx and Leica Application Suite (version 4.9.0) imaging software
270 (Leica Microsystems, Buffalo Grove, IL, USA). Images were processed with Panoramic Viewer (3DHISTECH,
271 Budapest, Hungary) and Photoshop (Adobe, San Jose, CA, USA) software.

272 ***Antibody validation and conjugation to metal isotopes for IMC.***

273 Several lanthanide-conjugated antibodies were purchased from Fluidigm (Markham, ON, Canada). Antibodies not
274 available in metal-conjugated form were purchased in carrier-free solution and validated by brightfield
275 immunohistochemistry using the appropriate isotype control antibodies. Subsequently, antibodies were conjugated to
276 lanthanide metal isotopes following the Maxpar® Antibody Labeling Kit protocol (Fluidigm). Metal-conjugated
277 antibodies were stored at 0.5 mg/mL in PBS-based Antibody Stabilizer (Candor Bioscience, Wangen, Germany) with
278 0.05% sodium azide at 4°C. Working concentrations for all metal-conjugated antibodies were optimized by IMC
279 (Table 2) on MS lesion tissue.

280 ***Imaging mass cytometry.***

281 For IMC histology, tissue sections were de-paraffinized and rehydrated, and antigen retrieval was performed in pH 8,
282 1 mM EDTA buffer at 96°C for 20 minutes. Sections were cooled at room temperature and rinsed in tap water and
283 TBS (20 mM Tris with 500 mM NaCl, pH 7.5). Tissue was blocked for 3 hours at room temperature with 0.3% BSA,
284 25% FBS and 0.1 mg/mL FC receptor binding inhibitor in TBS-T (TBS + 0.05% Tween-20). All antibodies (Table 2)
285 were diluted in 0.3% BSA in TBS-T and applied to the tissue for overnight incubation at 4°C. Sections were then
286 rinsed in TBS-T and TBS, and counterstained with 125 nM Maxpar® Intercalator-Ir (Fluidigm) in PBS for 1 hour at
287 room temperature. Sections were rinsed in TBS-T, TBS and two washes of distilled water before air-drying at room
288 temperature. Antibody-labeled tissue areas (1000x1000 µm) were raster-ablated using a Hyperion™ Laser Scanning
289 Module (Fluidigm) with a 1 µm diameter spot size at 200 Hz. This process was coupled to a Helios™ Mass Cytometer
290 (Fluidigm) for lanthanide metal detection [35]. Images for each antibody channel were acquired on CyTOF Software
291 (Fluidigm, version 6.7). MCD Viewer (Fluidigm, version 1.0) was used to export raw 16-bit tiff images for
292 computational analyses on histoCAT (version 1.75) [29]. For visualization purposes, images were processed in MCD
293 Viewer and ImageJ [31].

294 ***Computational analyses.***

295 *Single-cell segmentation.* Merged CD68 (macrophages/microglia), S100B (astrocytes), and CD3 (T cells) antibody
296 channel images were used to segment single cell objects on CellProfiler (version 3.0.0) [11]. The resulting
297 segmentation mask images, which outline cell borders, were loaded into histoCAT with corresponding antibody
298 channel images.

299 *Identification of cellular phenotypes.* Mean single-cell marker intensity values were extracted from segmented
300 antibody channel images on histoCAT and Z-score normalized. Based on the expression intensities of thirteen markers
301 (Table 2), cell clusters were defined using the PhenoGraph algorithm [15] integrated into histoCAT. Default
302 parameters with 75 nearest neighbors for the early lesion and 50 nearest neighbors for the late lesion were used. These
303 nearest neighbor values were chosen such that over- and under-clustering of phenotypes were avoided. Additional
304 normalization steps were performed internally, as previously described [29].

305 *Analysis of cellular phenotypes.* To visualize clusters, the Barnes-Hut t-SNE algorithm implemented in histoCAT was
306 executed with the same image and marker inputs used in PhenoGraph, as well as default parameters (initial
307 dimensions, 110; perplexity, 30; theta, 0.5) and internal normalization [1,29]. t-SNE plots were colored to highlight
308 clusters or show relative marker expression intensity. Images of cell phenotypes visualized in the tissue, as well as
309 segmentation masks overlaid with histology images, were generated in histoCAT. For the remaining analyses, ".csv"
310 files containing single-cell parameters were exported from histoCAT and appropriately processed for their application.
311 To produce an expression heatmap for clusters, normalized marker intensity values were processed using the R
312 *ComplexHeatmap* package, which hierarchically clusters single cells within clusters using Ward's method [30]. Violin
313 plots showing single-cell marker expression variability for each cluster were generated using the R *ggplot2* package
314 [9]. To study phenotype transitions, Potential of Heat-diffusion Affinity-based Transition Embedding (PHATE)
315 mapping and Monocle Pseudotime analyses were performed [19,26,27,33]. PHATE mapping was performed using
316 normalized marker intensity values, with an adjusted number of nearest neighbors ($k = 100$) and other parameters left
317 as their default specifications. Pseudotime analysis was performed with negative binomial normalization of marker
318 intensity values and $q < 1$ to incorporate all markers, based on a test for differential expression among phenotypes.
319 Figures showing phenotype cell size and relative quantity of cells per cluster, as well as correlation matrices and
320 corresponding marker scatter plots with linear regression lines were produced in Prism (version 7). FlowJo software
321 (version 10.5.3) was used to visualize single-cell marker data on flow cytometry plots. Images and figures were
322 recolored when necessary in Photoshop.

323 *Analysis of cell spatial relationships.* To study the spatial relationships of cell clusters, neighborhood analysis was
324 performed on histoCAT using the PhenoGraph-generated clusters pertaining to each lesion. Significant pairwise
325 phenotype interactions and avoidances were determined by an unbiased permutation test which compared the
326 frequency of one cell type neighboring another to the frequency in 999 random permutations of cell cluster labels.

327 Neighbors were identified within 4 μm from each cell, and neighboring frequency was normalized to the number of
328 interacting cells [29]. Analyses were performed for different degrees of significance ($p < 0.05$ and $p < 0.01$), and the
329 results were reported on a heatmap. To identify sources of single-cell marker variation, spatial variance component
330 analysis (SVCA) [2] was performed on Python for different lesion zones, using standardized marker intensity values.
331 SVCA plots were generated in R and Prism.

332 *Statistical analyses.* In plots showing phenotype cell size, data represent mean cell areas + standard deviation.
333 Comparisons of phenotype cell sizes were analyzed by one-way ANOVA followed by the Tukey-Kramer multiple
334 comparison test. Comparisons of two samples were carried out by unpaired Student's t-tests. For correlation analyses,
335 Pearson correlation coefficients were computed. $*p < 0.0001$.

336

337 **Figure supplement list**

338 Figure 3—figure supplement 1: Imaging mass cytometry histology images of the early lesion
339 Figure 3—figure supplement 2: Early lesion cell phenotype frequency and size
340 Figure 4—figure supplement 1: PHATE mapping of astrocyte phenotypes in the early lesion
341 Figure 5—figure supplement 1: Imaging mass cytometry histology images of the late lesion
342 Figure 5—figure supplement 2: Late lesion cell phenotype frequency and size
343 Figure 6—figure supplement 1: PHATE mapping of astrocyte phenotypes in the late lesion
344 Figure 7—figure supplement 1: Pearson correlation matrices for myeloid cells and astrocytes

345

346 **Data availability**

347 Source data generated and/or analyzed during the current study as well as R source code are available in a GitHub
348 repository: https://github.com/PittLab/IMC_Park_et_al_2019.

349

350 **Acknowledgments**

351 The authors thank Fluidigm Corporation (Markham, ON, Canada) and the Yale University CyTOF core facility for
352 providing IMC tissue imaging service and metal-conjugated antibodies, as well as Denis Schapiro, Damien Arnol and
353 Kevin Moon for expert assistance with computational analyses.

354 **References**

355 1. Amir E-aD, Davis KL, Tadmor MD, Simonds EF, Levine JH, Bendall SC, Shenfeld DK, Krishnaswamy S, Nolan
356 GP, Pe'er D (2013) viSNE enables visualization of high dimensional single-cell data and reveals phenotypic
357 heterogeneity of leukemia. Nature Biotechnology 31:545. doi:10.1038/nbt.2594
358 2. Arnol D, Schapiro D, Bodenmiller B, Saez-Rodriguez J, Stegle O (2018) Modelling cell-cell interactions from
359 spatial molecular data with spatial variance component analysis. bioRxiv:265256. doi:10.1101/265256
360 3. Bartnik BL, Juurlink BH, Devon RM (2000) Macrophages: their myelinotrophic or neurotoxic actions depend upon
361 tissue oxidative stress. Multiple sclerosis (Houndmills, Basingstoke, England) 6:37-42.
362 doi:10.1177/135245850000600108
363 4. Bolognesi MM, Manzoni M, Scalia CR, Zannella S, Bosisio FM, Faretta M, Cattoretti G (2017) Multiplex Staining
364 by Sequential Immunostaining and Antibody Removal on Routine Tissue Sections. The journal of
365 histochemistry and cytochemistry : official journal of the Histochemistry Society 65:431-444.
366 doi:10.1369/0022155417719419
367 5. Boven LA, Van Meurs M, Van Zwam M, Wierenga-Wolf A, Hintzen RQ, Boot RG, Aerts JM, Amor S,
368 Nieuwenhuis EE, Laman JD (2006) Myelin-laden macrophages are anti-inflammatory, consistent with foam
369 cells in multiple sclerosis. Brain : a journal of neurology 129:517-526. doi:10.1093/brain/awh707
370 6. Farina C, Aloisi F, Meinl E (2007) Astrocytes are active players in cerebral innate immunity. Trends in immunology
371 28:138-145. doi:10.1016/j.it.2007.01.005
372 7. Giles DA, Washnock-Schmid JM, Duncker PC, Dahlawi S, Ponath G, Pitt D, Segal BM (2018) Myeloid cell
373 plasticity in the evolution of central nervous system autoimmunity. Annals of neurology 83:131-141.
374 doi:10.1002/ana.25128
375 8. Gut G, Herrmann MD, Pelkmans L (2018) Multiplexed protein maps link subcellular organization to cellular states.
376 Science 361:eaar7042. doi:10.1126/science.aar7042
377 9. Hadley W (2016) ggplot2: Elegant Graphics for Data Analysis. Springer-Verlag New York,
378 10. Jakel S, Agirre E, Mendanha Falcao A, van Bruggen D, Lee KW, Knuesel I, Malhotra D, Ffrench-Constant C,
379 Williams A, Castelo-Branco G (2019) Altered human oligodendrocyte heterogeneity in multiple sclerosis.
380 Nature 566:543-547. doi:10.1038/s41586-019-0903-2
381 11. Kamentsky L, Jones TR, Fraser A, Bray MA, Logan DJ, Madden KL, Ljosa V, Rueden C, Eliceiri KW, Carpenter
382 AE (2011) Improved structure, function and compatibility for CellProfiler: modular high-throughput image
383 analysis software. Bioinformatics (Oxford, England) 27:1179-1180. doi:10.1093/bioinformatics/btr095
384 12. Kim CC, Nakamura MC, Hsieh CL (2016) Brain trauma elicits non-canonical macrophage activation states. J
385 Neuroinflammation 13:117. doi:10.1186/s12974-016-0581-z
386 13. Kuhlmann T, Ludwin S, Prat A, Antel J, Brück W, Lassmann H (2017) An updated histological classification
387 system for multiple sclerosis lesions. Acta Neuropathologica 133:13-24. doi:10.1007/s00401-016-1653-y
388 14. Lassmann H (2018) Multiple Sclerosis Pathology. Cold Spring Harbor perspectives in medicine 8.
389 doi:10.1101/cshperspect.a028936
390 15. Levine JH, Simonds EF, Bendall SC, Davis KL, Amir el AD, Tadmor MD, Litvin O, Fienberg HG, Jager A,
391 Zunder ER, Finck R, Gedman AL, Radtke I, Downing JR, Pe'er D, Nolan GP (2015) Data-Driven Phenotypic
392 Dissection of AML Reveals Progenitor-like Cells that Correlate with Prognosis. Cell 162:184-197.
393 doi:10.1016/j.cell.2015.05.047
394 16. Locatelli G, Theodorou D, Kendirli A, Jordao MJC, Staszewski O, Phulphagar K, Cantuti-Castelvetri L, Dagkalis
395 A, Bessis A, Simons M, Meissner F, Prinz M, Kerschensteiner M (2018) Mononuclear phagocytes locally
396 specify and adapt their phenotype in a multiple sclerosis model. Nature neuroscience 21:1196-1208.
397 doi:10.1038/s41593-018-0212-3
398 17. Love S, Louis D, Ellison DW, Sobel RA, Moore GRW (2008) Chapter 20: Demyelinating diseases. In: Greenfield's
399 Neuropathology. Boca Raton, FL: CRC Press; p. 1526.
400 18. Mayo L, Trauger SA, Blain M, Nadeau M, Patel B, Alvarez JI, Mascanfroni ID, Yeste A, Kivisakk P, Kallas K,
401 Ellezam B, Bakshi R, Prat A, Antel JP, Weiner HL, Quintana FJ (2014) Regulation of astrocyte activation
402 by glycolipids drives chronic CNS inflammation. Nature medicine 20:1147-1156. doi:10.1038/nm.3681
403 19. Moon KR, van Dijk D, Wang Z, Gigante S, Burkhardt D, Chen W, van den Elzen A, Hirn MJ, Coifman RR,
404 Ivanova NB, Wolf G, Krishnaswamy S (2018) Visualizing Transitions and Structure for Biological Data
405 Exploration. bioRxiv:120378. doi:10.1101/120378
406 20. Mrdjen D, Pavlovic A, Hartmann FJ, Schreiner B, Utz SG, Leung BP, Lelios I, Heppner FL, Kipnis J, Merkler D,
407 Greter M, Becher B (2018) High-Dimensional Single-Cell Mapping of Central Nervous System Immune

Cells Reveals Distinct Myeloid Subsets in Health, Aging, and Disease. Immunity 48:380-395.e386. doi:10.1016/j.immuni.2018.01.011

21. Nylander A, Hafler DA (2012) Multiple sclerosis. The Journal of clinical investigation 122:1180-1188. doi:10.1172/jci58649
22. Pitt D, Nagelmeier IE, Wilson HC, Raine CS (2003) Glutamate uptake by oligodendrocytes: Implications for excitotoxicity in multiple sclerosis. Neurology 61:1113-1120
23. Ponath G, Lincoln MR, Levine-Ritterman M, Park C, Dahlawi S, Mubarak M, Sumida T, Airas L, Zhang S, Isitan C, Nguyen TD, Raine CS, Hafler DA, Pitt D (2018) Enhanced astrocyte responses are driven by a genetic risk allele associated with multiple sclerosis. Nature Communications 9:5337. doi:10.1038/s41467-018-07785-8
24. Ponath G, Park C, Pitt D (2018) The Role of Astrocytes in Multiple Sclerosis. Frontiers in immunology 9:217-217. doi:10.3389/fimmu.2018.00217
25. Prineas J (1975) Pathology of the early lesion in multiple sclerosis. Human pathology 6:531-554
26. Qiu X, Hill A, Packer J, Lin D, Ma YA, Trapnell C (2017) Single-cell mRNA quantification and differential analysis with Census. Nature methods 14:309-315. doi:10.1038/nmeth.4150
27. Qiu X, Mao Q, Tang Y, Wang L, Chawla R, Pliner HA, Trapnell C (2017) Reversed graph embedding resolves complex single-cell trajectories. Nature methods 14:979-982. doi:10.1038/nmeth.4402
28. Ransohoff RM (2016) A polarizing question: do M1 and M2 microglia exist? Nature neuroscience 19:987. doi:10.1038/nn.4338
29. Schapiro D, Jackson HW, Raghuraman S, Fischer JR, Zanotelli VRT, Schulz D, Giesen C, Catena R, Varga Z, Bodenmiller B (2017) histoCAT: analysis of cell phenotypes and interactions in multiplex image cytometry data. Nature methods 14:873-876. doi:10.1038/nmeth.4391
30. Schlesner M, Gu Z, Eils R (2016) Complex heatmaps reveal patterns and correlations in multidimensional genomic data. Bioinformatics (Oxford, England) 32:2847-2849. doi:10.1093/bioinformatics/btw313
31. Schneider CA, Rasband WS, Eliceiri KW (2012) NIH Image to ImageJ: 25 years of image analysis. Nature methods 9:671-675
32. Tanaka R, Iwasaki Y, Koprowski H (1975) Ultrastructural studies of perivascular cuffing cells in multiple sclerosis brain. The American journal of pathology 81:467-478
33. Trapnell C, Cacchiarelli D, Grimsby J, Pokharel P, Li S, Morse M, Lennon NJ, Livak KJ, Mikkelsen TS, Rinn JL (2014) The dynamics and regulators of cell fate decisions are revealed by pseudotemporal ordering of single cells. Nat Biotechnol 32:381-386. doi:10.1038/nbt.2859
34. Vogel DYS, Vereyken EJF, Glim JE, Heijnen PDAM, Moeton M, van der Valk P, Amor S, Teunissen CE, van Horssen J, Dijkstra CD (2013) Macrophages in inflammatory multiple sclerosis lesions have an intermediate activation status. Journal of neuroinflammation 10:35-35. doi:10.1186/1742-2094-10-35
35. Wang HA, Grolimund D, Giesen C, Borca CN, Shaw-Stewart JR, Bodenmiller B, Gunther D (2013) Fast chemical imaging at high spatial resolution by laser ablation inductively coupled plasma mass spectrometry. Analytical chemistry 85:10107-10116. doi:10.1021/ac400996x

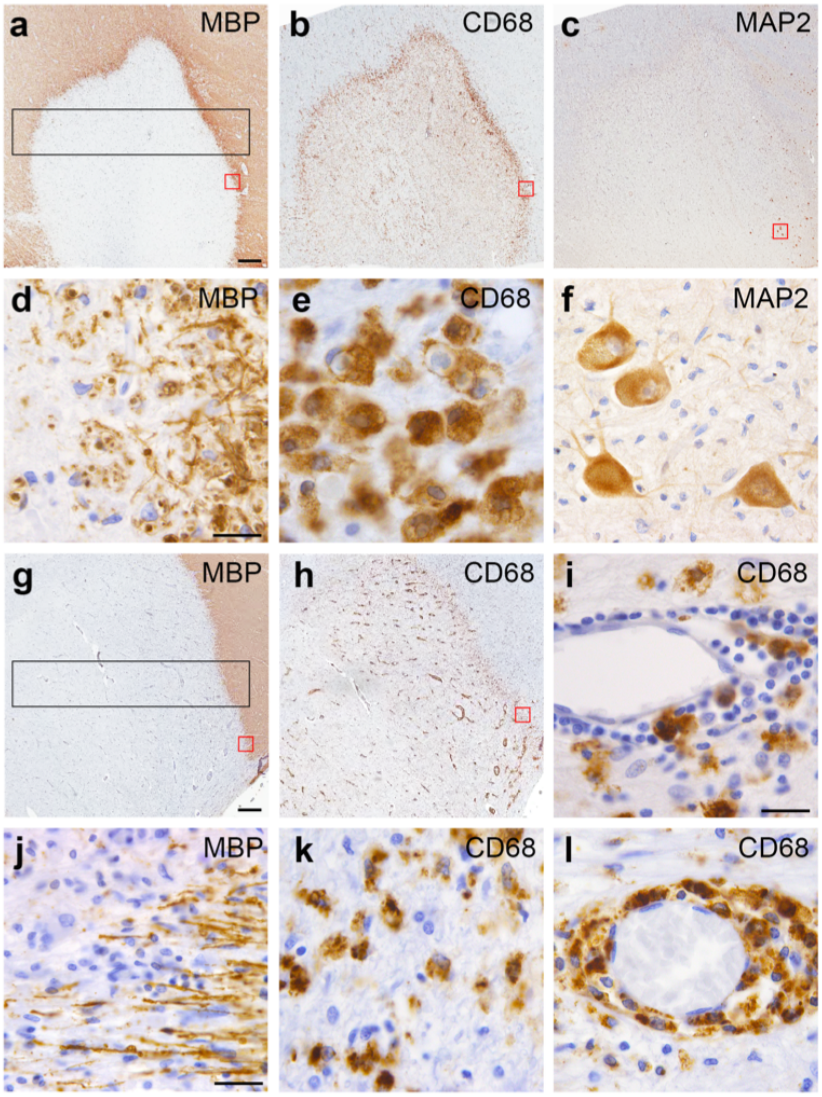

Figure 1 Brightfield images of the MS lesions examined with IMC. **(a-f, i)** Staining of the early, actively demyelinating lesion for **(a)** myelin basic protein (MBP), **(b)** CD68 (macrophages/microglia) and **(c)** the neuronal marker MAP2. The black rectangle in **(a)** shows the region that was laser-ablated for IMC, capturing the NAWM, hypercellular rim on both sides and lesion center. Red boxes in **a-c** correspond to magnified rim areas in **d-f,** demonstrating in **(d)** condensed myelin fragments, indicative of ongoing demyelination, **(e)** dense infiltration with foamy macrophages and **(f)** dispersed neuronal cell bodies in the right lesion rim.
(g, h, j-l) Staining against MBP and CD68 in the late, post-demyelinating lesion. The black rectangle in **(g)** shows the region laser-ablated for IMC. **(j, k)** Details from **(g)** and **(h)** showing absence of myelin fragments and reduced myeloid cell density at the lesion rim compared to **(e)**. $CD68^+$ cells in the perivascular spaces of **(i)** the early lesion and **(l)** the late lesion. Images show hematoxylin counterstaining. Scale bars **a-c, g, h** = 500 µm. Scale bars **d-f, i, j-l** = 25 µm.

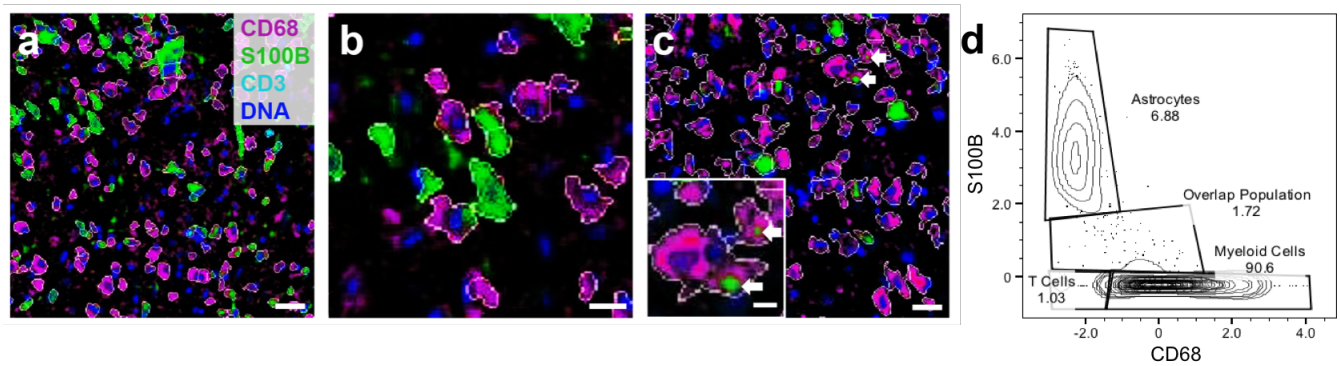

Figure 2 Single-cell segmentation. **(a-c)** Segmentation of myeloid cells (CD68, magenta), astrocytes (S100B, green) and T cells (CD3, cyan) performed on CellProfiler. **(b)** shows cells in **(a)** at higher magnification. **(c)** shows examples of $S100B^+$ astrocyte processes (white arrows) that closely neighbor $CD68^+$ cells, which resulted in the co-segmentation of these markers in a small fraction of cells. **(d)** Gating of $CD68^+$ and $S100B^+$ populations on a flow cytometry plot as a quality control for segmentation. The overlap population consists of cells with co-segmented CD68 and S100B like those in **(c)**. Scale bar in **(a)** = 30 µm; **(b)** = 15 µm; **(c)** = 30 µm, inset = 10 µm. Z-score normalized expression intensities are shown **(d)**. CellProfiler segmentation files and corresponding IMC histology images are available in a GitHub repository (see data availability statement).

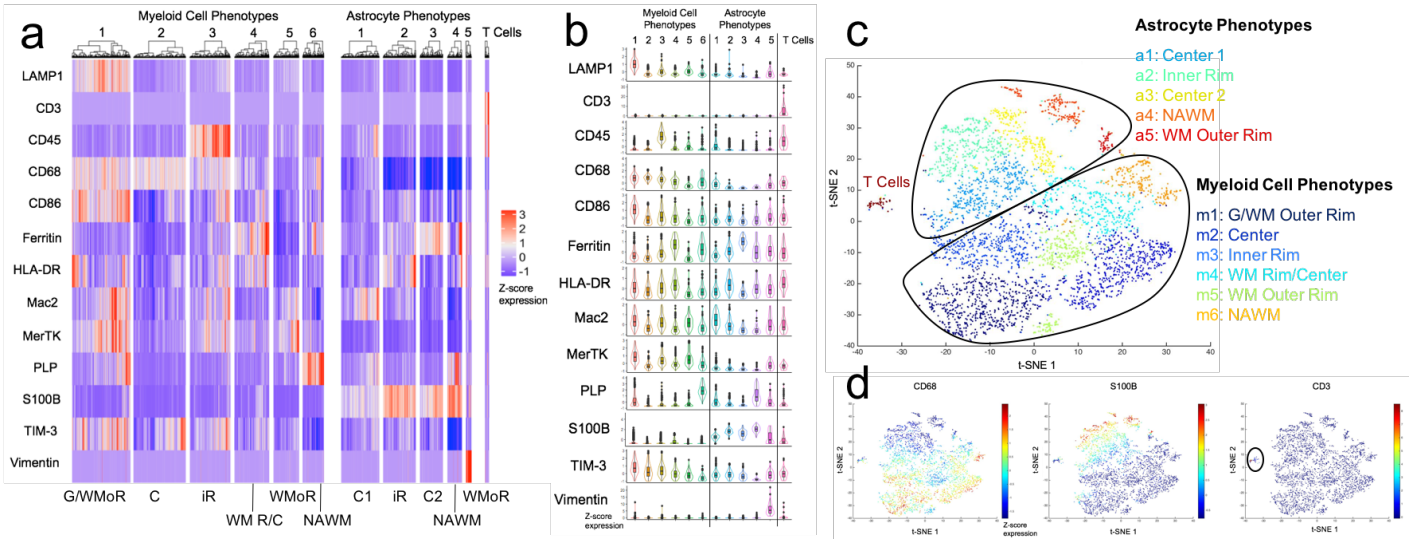

Figure 3 Early lesion cell phenotype profiles. **(a)** Marker expression heatmap for the myeloid, astrocyte and T cell phenotypes, identified by PhenoGraph clustering on histoCAT using segmented cells (n = 4397). The heatmap displays relative expression levels based on Z-score normalized marker intensity values, and single cells are hierarchically clustered within each phenotype group. Labels at the bottom of the heatmap indicate the area of the lesion to which each phenotype localizes. **(b)** Violin plot representation of the data in **(a)**. **(c)** t-SNE plot showing the distinct phenotype clusters. **(d)** t-SNE plot colored by marker intensity, confirming the separation of $CD68^+$, $S100B^+$ and $CD3^+$ cell types. G/WMoR = gray and white matter outer rim; WMoR = white matter outer rim; iR = inner rim; WM R/C = white matter rim/center; C = center; NAWM = normal-appearing white matter. Source single-cell and histoCAT session data are available in a GitHub repository (see data availability statement).

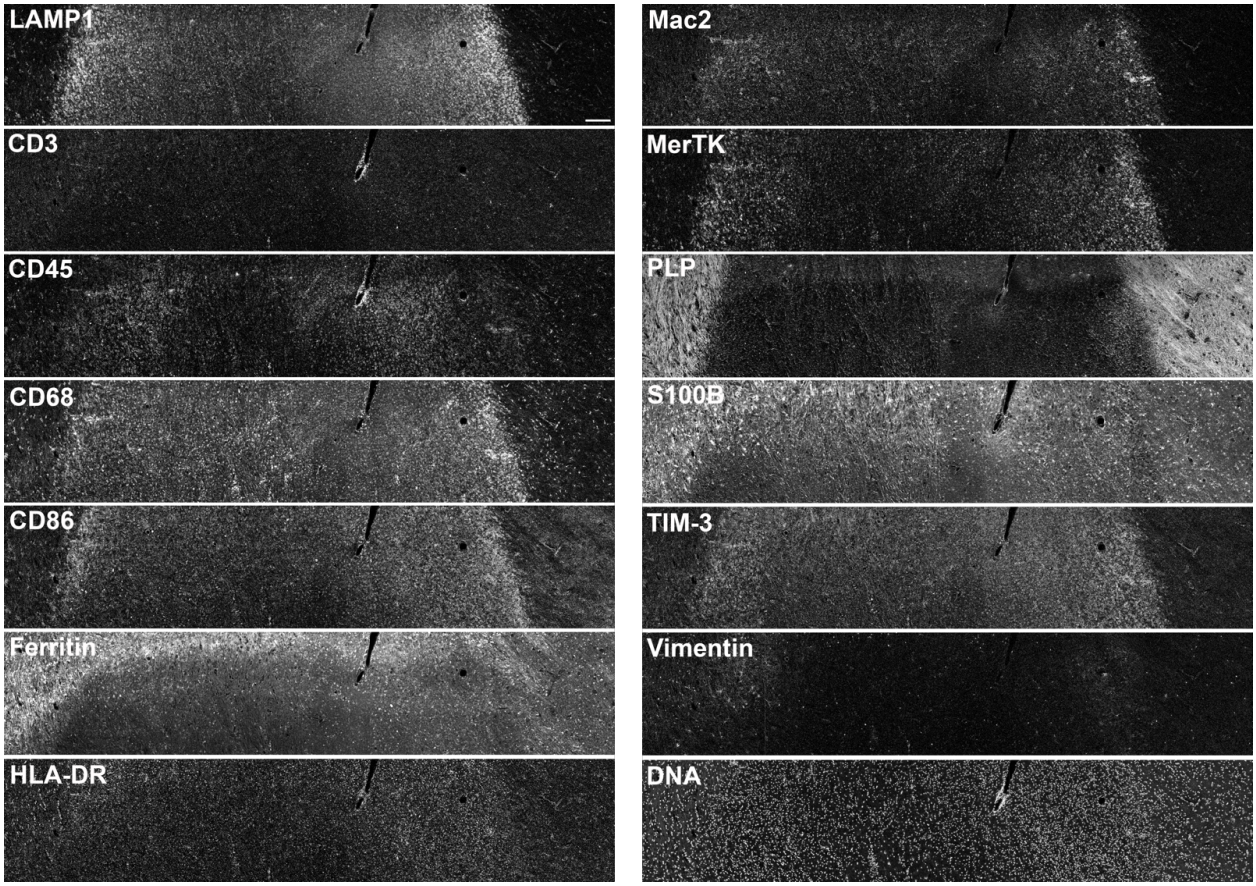

Figure 3—figure supplement 1 Imaging mass cytometry histology images of the early lesion. The thirteen markers used for cell clustering as well as DNA counterstaining are shown. Scale bar = 200 µm.

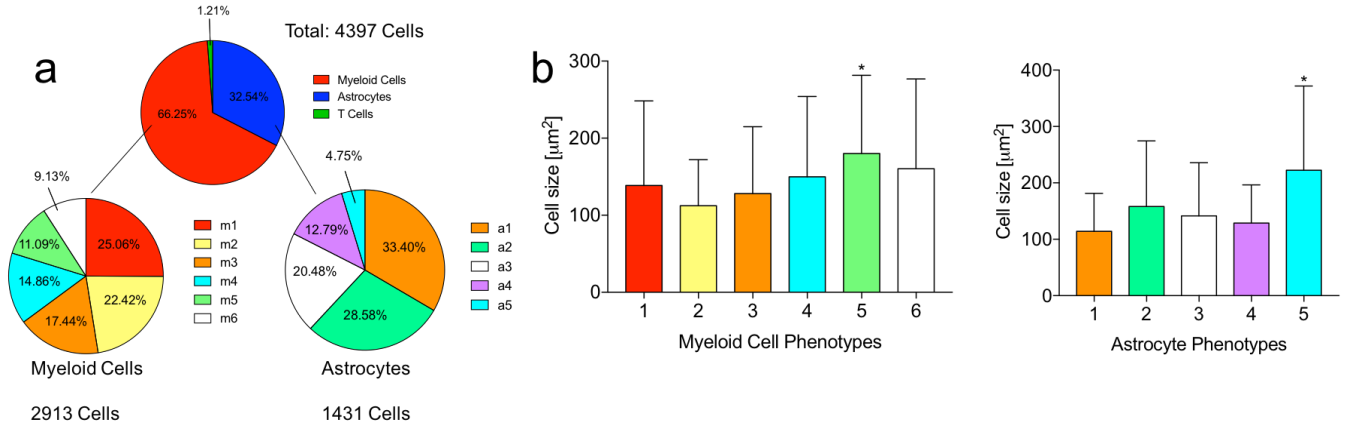

Figure 3—figure supplement 2 Early lesion cell phenotype frequency and size. **(a)** Relative quantities of each cell phenotype. **(b)** Cell phenotype size. Data represent means + standard deviation. *$p < 0.0001$ by one-way ANOVA followed by the Tukey-Kramer multiple comparison test. Source data is available in a GitHub repository (see data availability statement).

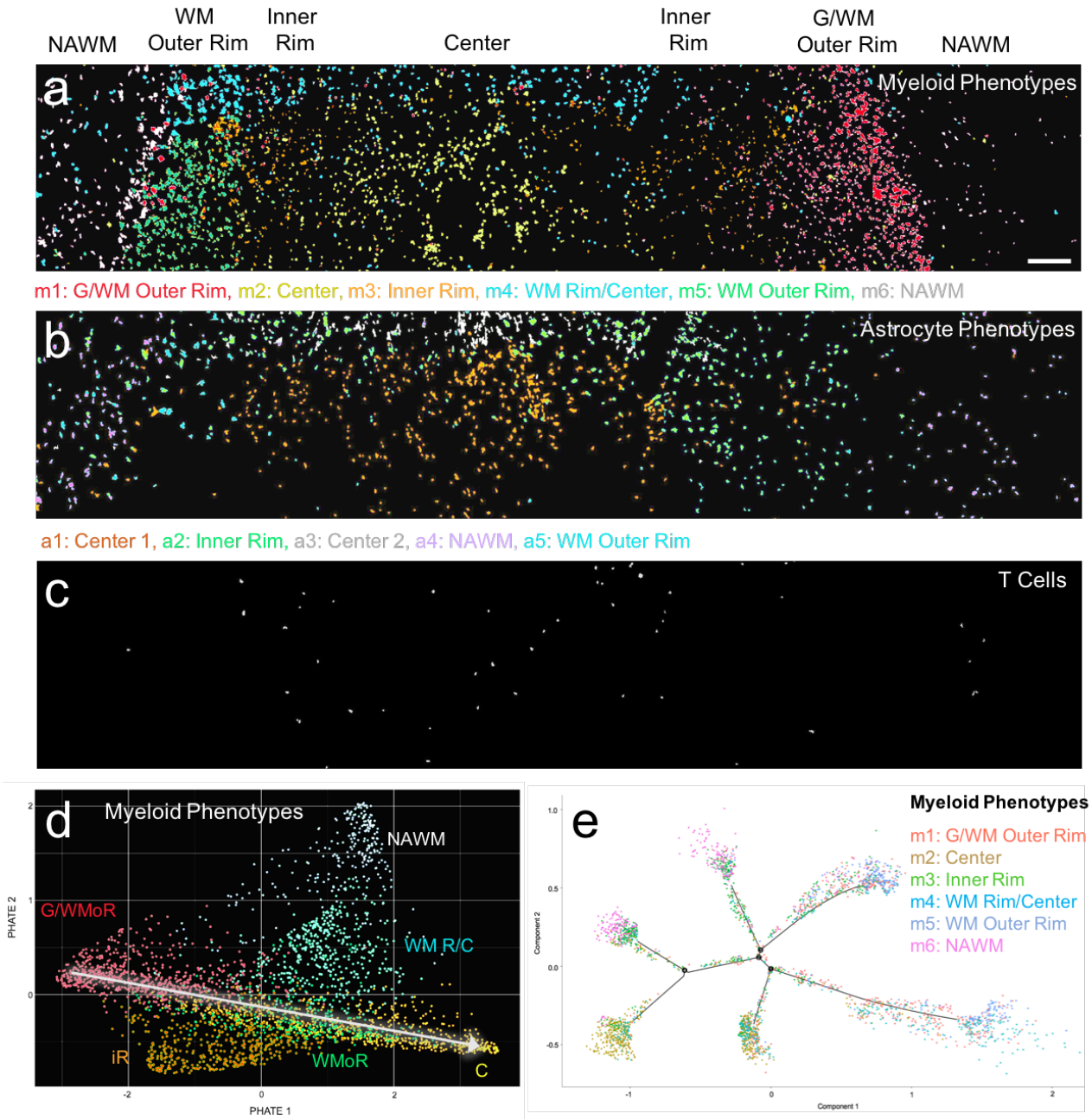

Figure 4 Early lesion phenotype spatial distributions and transition analyses. **(a, b)** Spatial separation of **(a)** myeloid cell and **(b)** astrocyte phenotypes into NAWM, rim and center lesion zones. **(c)** T cells are primarily located in the lesion center. **(d)** PHATE mapping of myeloid cells, indicating that the G/WM outer rim (m1) and lesion center phenotypes (m2) are on a transition continuum (white arrow). **(e)** Pseudotime analysis of myeloid cells shows that phenotypes transition along independent trajectories. Phenotype color schemes on the PHATE and Pseudotime plots reflect the color palettes specific to each analysis. Scale bar for **a-c** = 200 µm. G/WMoR = gray and white matter outer rim; WMoR = white matter outer rim; iR = inner rim; WM R/C = white matter rim/center; C = center; NAWM = normal-appearing white matter. Source data is available in a GitHub repository (see data availability statement).

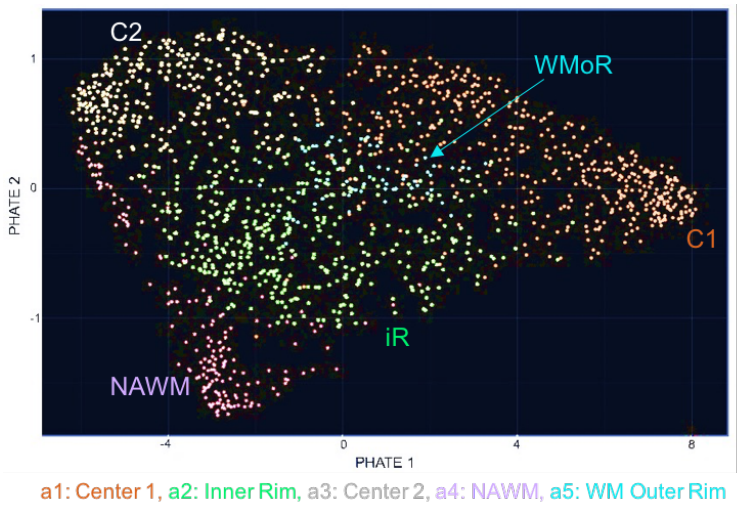

Figure 4—figure supplement 1 PHATE mapping of astrocyte phenotypes in the early lesion. WMoR = white matter outer rim; iR = inner rim; C = center; NAWM = normal-appearing white matter. Source data is available in a GitHub repository (see data availability statement).

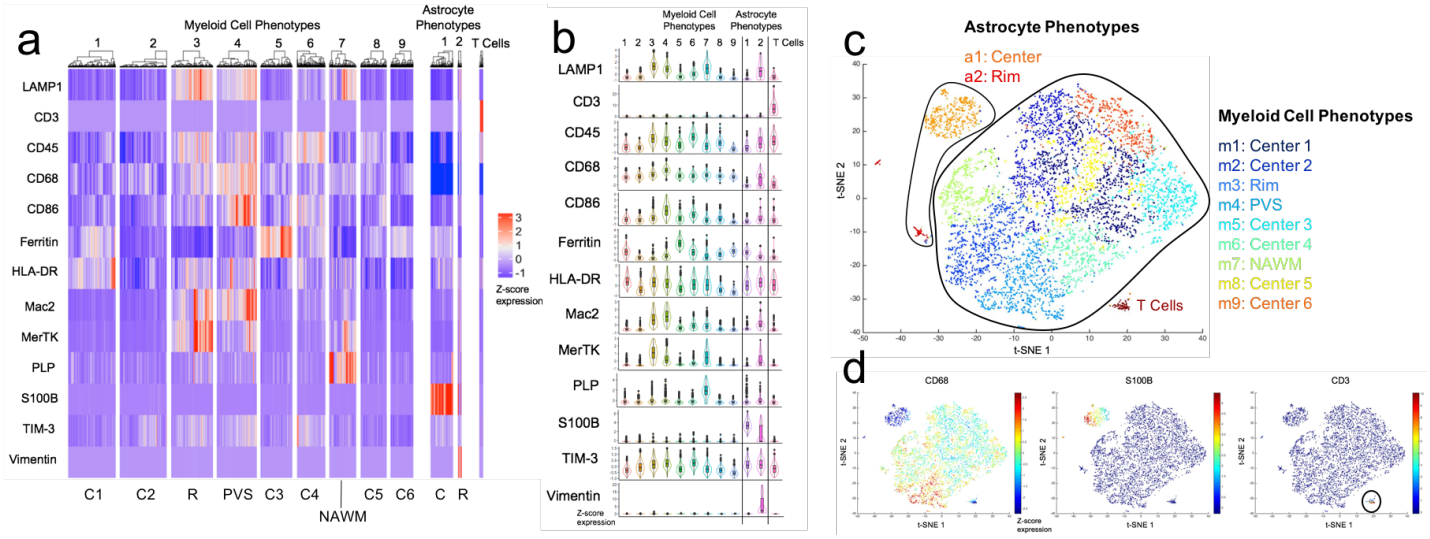

Figure 5 Late lesion cell phenotype profiles. **(a)** Marker expression heatmap for the myeloid, astrocyte and T cell phenotypes, identified by PhenoGraph clustering on histoCAT using segmented cells (n = 6698). The heatmap displays relative expression levels based on Z-score normalized marker intensity values, and single cells are hierarchically clustered within each phenotype group. Labels at the bottom of the heatmap indicate the area of the lesion to which each phenotype localizes. **(b)** Violin plot representation of the data in **(a)**. **(c)** t-SNE plot showing the phenotype clusters. Compared to the early lesion, myeloid cell phenotypes show a low degree of separation. **(d)** t-SNE plot colored by marker intensity, confirming the separation of $CD68^+$, $S100B^+$ and $CD3^+$ cell types. R = rim; C = center; PVS = perivascular space; NAWM = normal-appearing white matter. Source single-cell and histoCAT session data are available in a GitHub repository (see data availability statement).

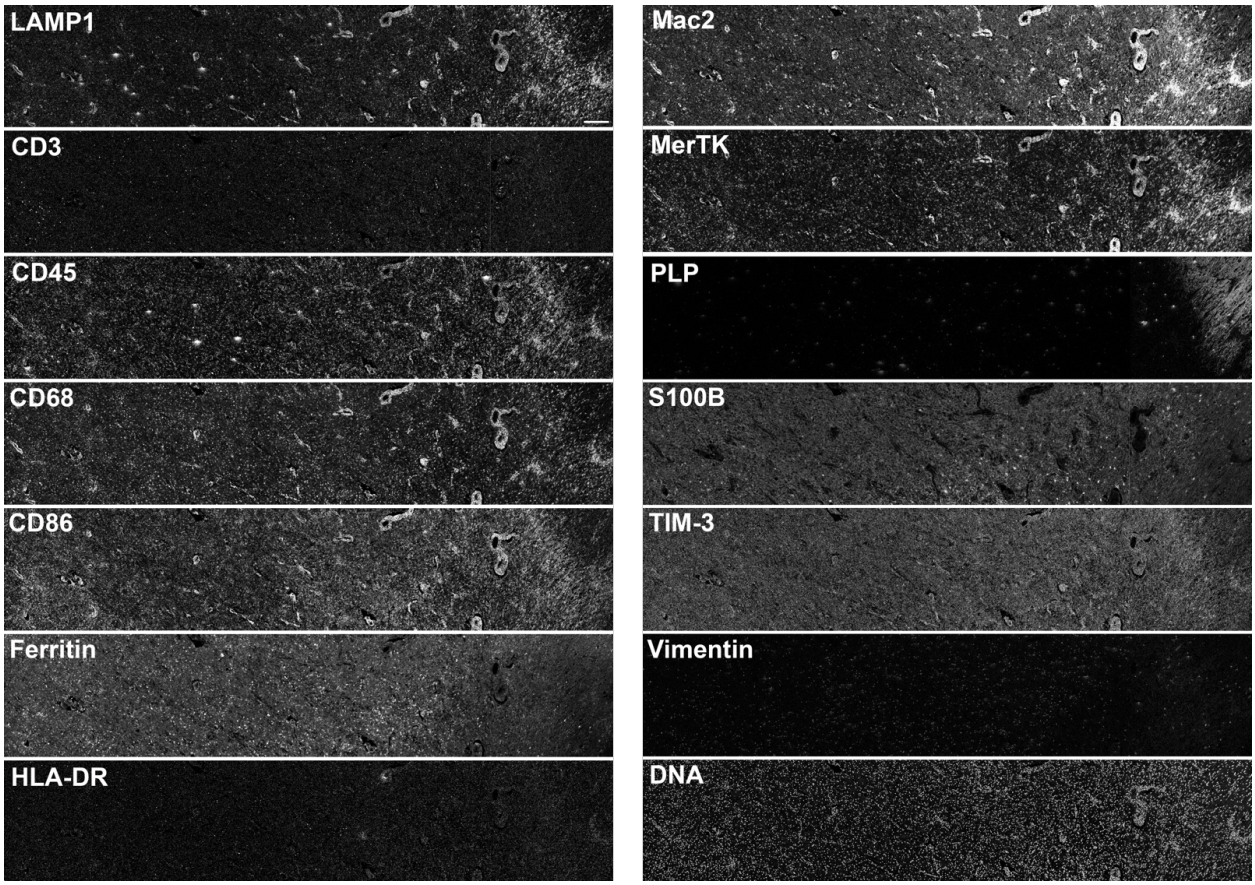

507
508 **Figure 5—figure supplement 1** Imaging mass cytometry histology images of the late lesion. The thirteen markers
509 used for cell clustering as well as DNA counterstaining are shown. Scale bar = 200 µm.

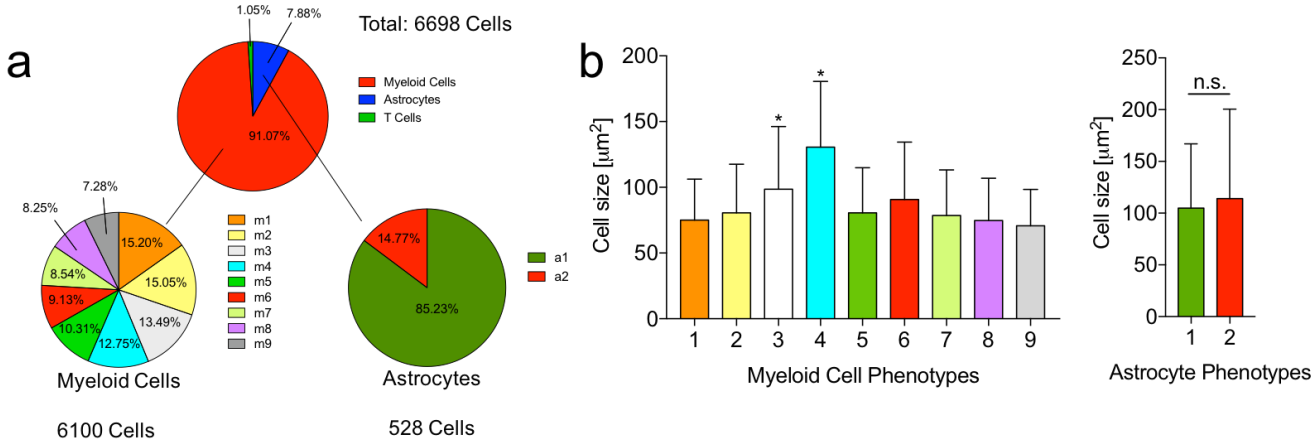

Figure 5—figure supplement 2 Late lesion cell phenotype frequency and size. **(a)** Relative quantities of each cell phenotype. **(b)** Cell phenotype size. Data represent means + standard deviation. *p < 0.0001 by one-way ANOVA followed by the Tukey-Kramer multiple comparison test. Source data is available in a GitHub repository (see data availability statement).

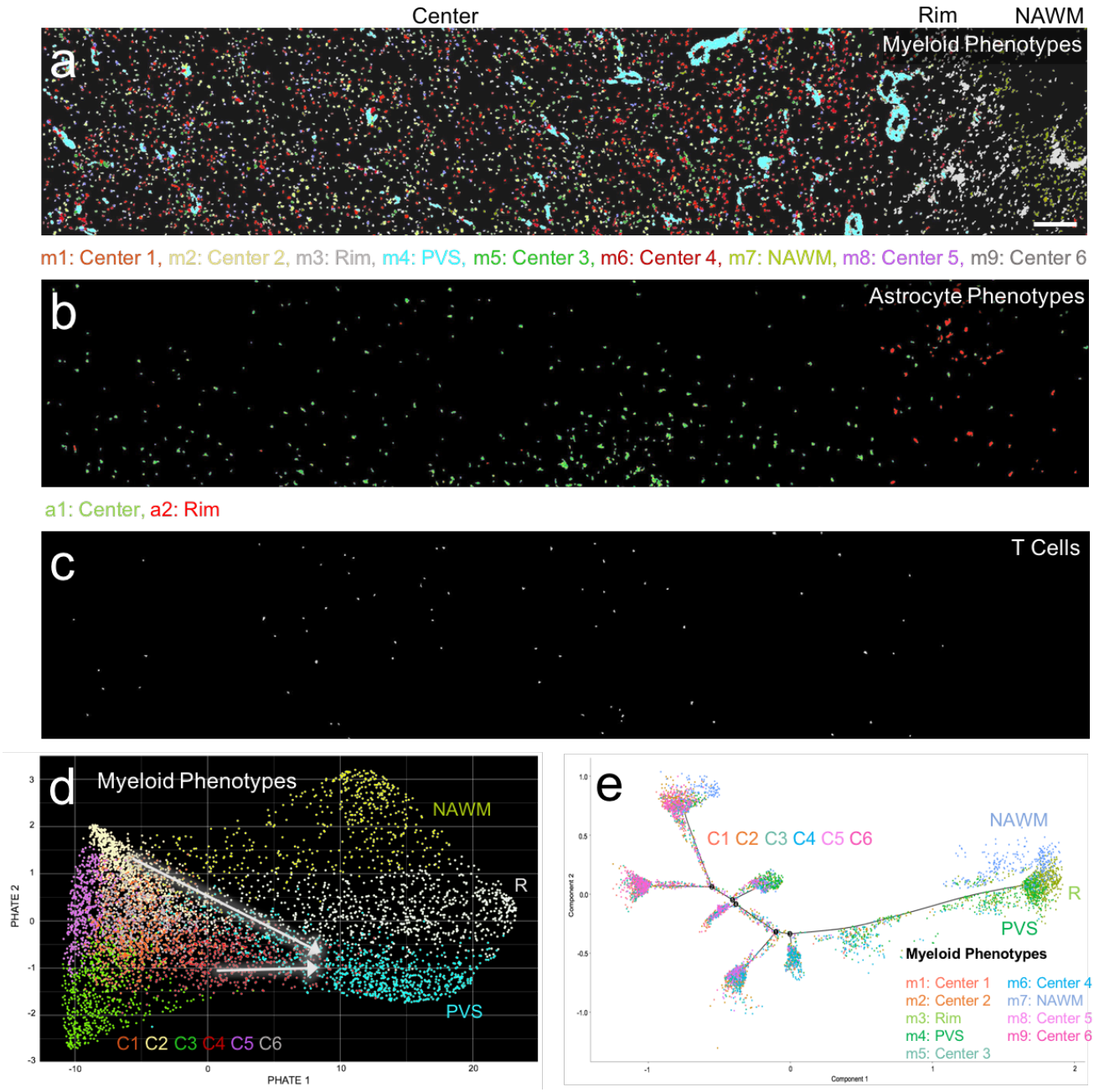

Figure 6 Late lesion phenotype spatial distributions and transition analyses. **(a)** Spatial organization of myeloid cell phenotypes in the lesion. Phenotypes in the rim (m3), perivascular space (m4) and NAWM (m7) separate into distinct zones, while lesion center phenotypes (m1, m2, m5, m6, m8, m9) are uniformly distributed. **(b)** Spatial distribution of astrocyte phenotypes. One phenotype (a1) predominantly occupies the lesion center and the other (a2) occupies the rim. **(c)** T cells are primarily distributed in the lesion center. **(d)** PHATE mapping of myeloid cells, showing that two lesion center phenotypes (m2, m6) are on a continuum with perivascular space cells (m4, white arrows). **(e)** Pseudotime analysis of myeloid cells shows a similar trajectory to PHATE mapping. Phenotype color schemes on the PHATE and Pseudotime plots reflect the color palettes specific to each analysis. Scale bar for **a-c** = 200 µm. R = rim; C = center; PVS = perivascular space; NAWM = normal-appearing white matter. Source data is available in a GitHub repository (see data availability statement).

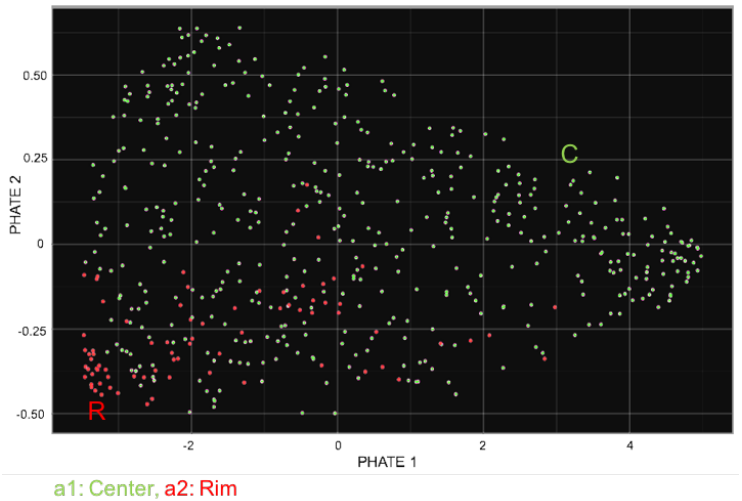

Figure 6—figure supplement 1 PHATE mapping of astrocyte phenotypes in the late lesion. R = rim; C = center. Source data is available in a GitHub repository (see data availability statement).

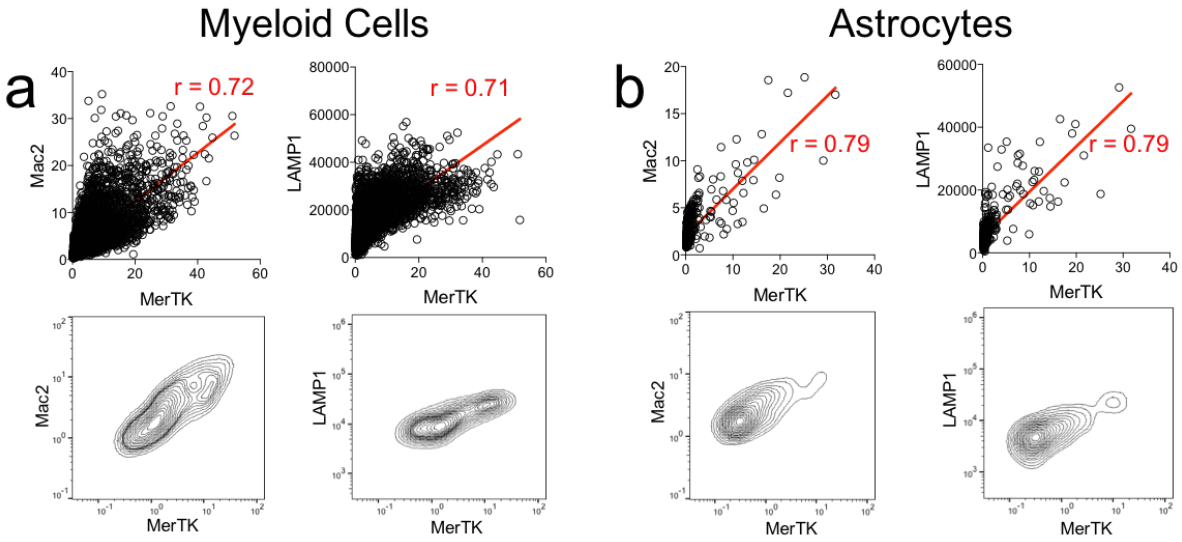

Figure 7 Single-cell marker correlations in the late lesion. **(a, b)** Co-expression of Mac2 and MerTK, and LAMP1 and MerTK in **(a)** myeloid cells (n = 6100), and **(b)** astrocytes (n = 528). Co-expression plots are shown with linear expression values and regression lines with Pearson correlation coefficients, and below in flow cytometry contour plot form with log10-transformed expression values. Source data is available in a GitHub repository (see data availability statement).

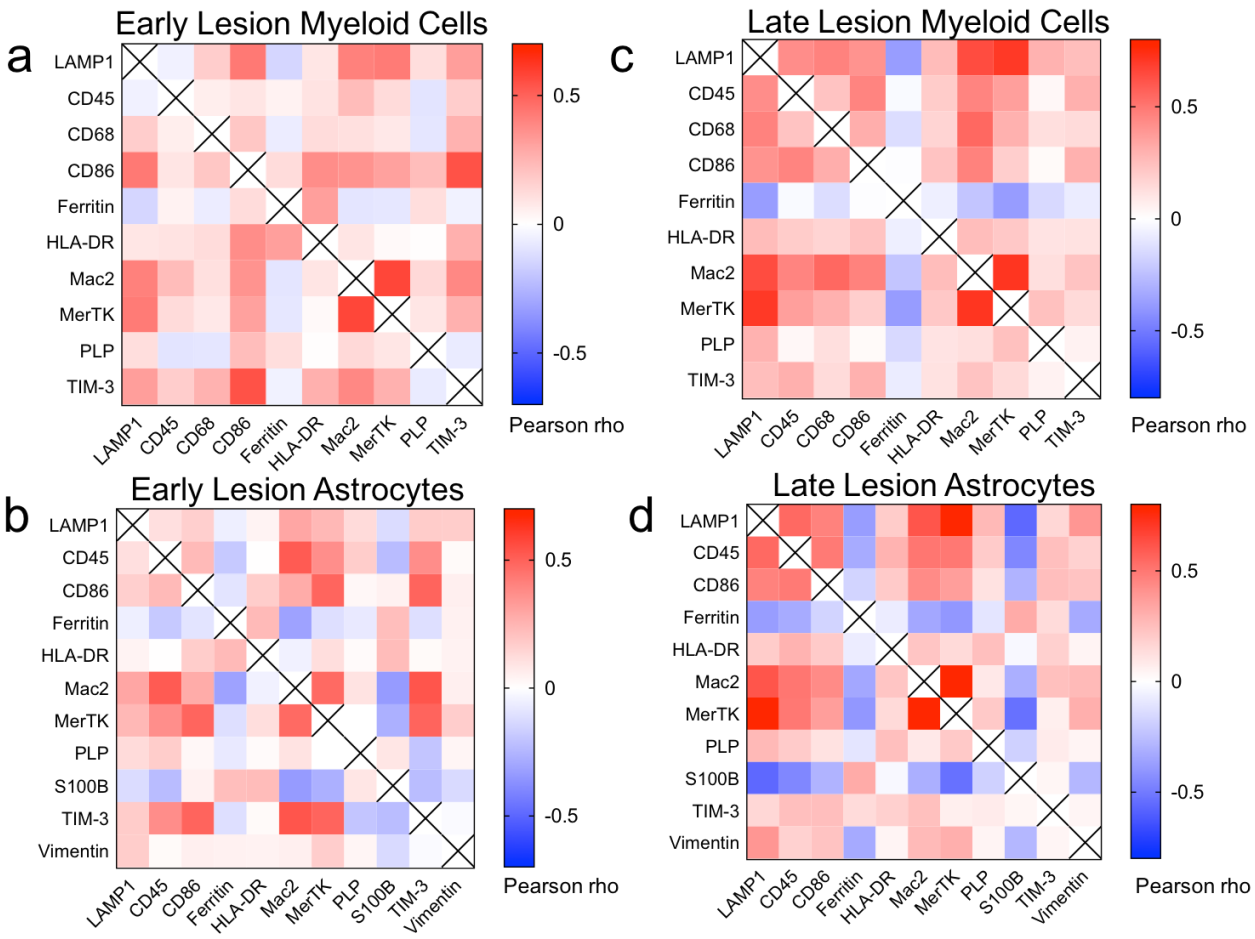

Figure 7—figure supplement 1 Pearson correlation matrices for myeloid cells and astrocytes. Matrices for early lesion **(a)** myeloid cells (n = 2913) and **(b)** astrocytes (n = 1431), and late lesion **(c)** myeloid cells (n = 6100) and **(d)** astrocytes (n = 528) are shown. Source data is available in a GitHub repository (see data availability statement).

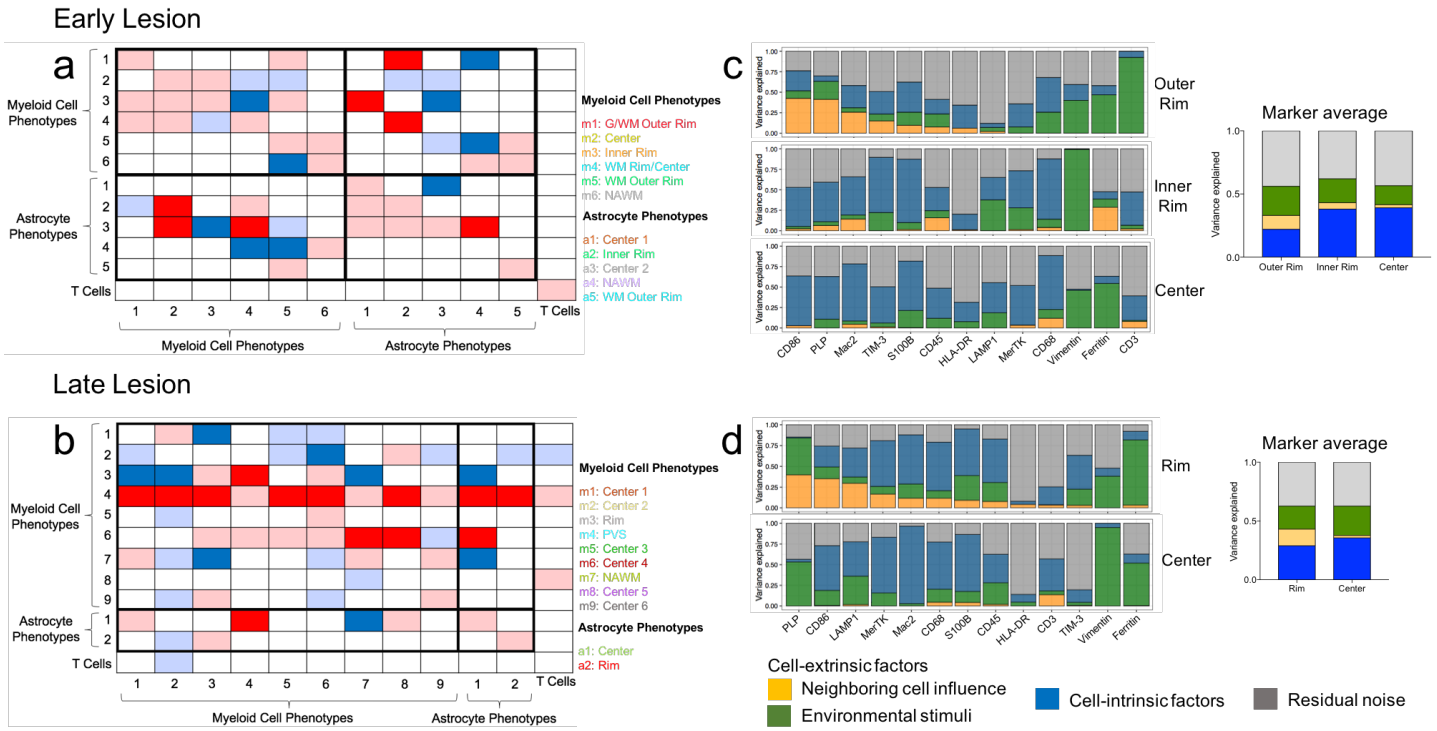

Figure 8 Neighborhood and spatial variance component analyses for the early and late lesions. **(a, b)** Neighborhood analysis heatmaps of all significant pairwise phenotype interactions (red) and avoidances (blue) in the **(a)** early and **(b)** late lesions. White represents no significant spatial relationship. Dark boxes are highly significant spatial relationships ($p < 0.01$). Lightly shaded boxes are less significant relationships ($p < 0.05$) and interactions between cells of the same or spatially adjacent phenotypes. Rows visualize the significance of a phenotype surrounded by other phenotypes, and columns visualize the significance of a phenotype surrounding other phenotypes. **(c, d)** Spatial variance component analysis (SVCA) for the **(c)** early and **(d)** late lesions, showing the proportion of marker expression variance attributable to neighboring cell influences, environmental stimuli, cell-intrinsic factors and residual noise in different lesion zones. Additional plots show the average proportion of marker variance attributable to each factor in different lesion zones. G/WM = gray and white matter; WM = white matter; PVS = perivascular space; NAWM = normal-appearing white matter. Source histoCAT session and SVCA data are available in a GitHub repository (see data availability statement).

552 **Table 1** Antibodies used for brightfield histology

Primary Antibody	Host	Clone	Company	Target/Significance	Primary Antibody Dilution	Secondary Antibody	Secondary Antibody Dilution
MBP	Rat	12	Millipore-Sigma	Myelin Basic Protein	1:500	Invitrogen, 629540	1:500
CD68	Rabbit	D4B9C	Cell Signaling	Activated macrophage/microglia transmembrane glycoprotein	1:500	Vector Laboratories, BA-1000	1:500
MAP2	Mouse	5H11	Novus	Neuron structural protein	1:200	Vector Laboratories, BA-9200	1:500

553 **Table 2** Metal-conjugated antibodies used for IMC

Antibody	Clone	Company	Target/Significance	Conjugated Metal Isotope	Conjugation Source	Dilution
LAMP1/CD107a	H4A3	Fluidigm	Lysosomes	151Eu	Fluidigm	1:100
CD3	Polyclonal	Fluidigm	T cells	170Er	Fluidigm	1:75
CD45	2B11	Fluidigm	Leukocyte activation	152Sm	Fluidigm	1:100
CD68	KP1	Fluidigm	Activated macrophages/microglia	159Tb	Fluidigm	1:300
CD86	Polyclonal	R&D	"M1" co-stimulatory molecule	171Yb	Our Lab	1:100
Ferritin heavy chain	1-2.3.1.2	Millipore-Sigma	Iron storage	158Gd	Our Lab	1:400
HLA-DR	YE2/36 HLK	Fluidigm	MHC Class II	174Yb	Fluidigm	1:200
Mac2	M3/38	Fluidigm	"M2" activation	153Eu	Fluidigm	1:600
MerTK	y323	abcam	"M2" phagocytosis	148Nd	Our Lab	1:50
PLP	plpc1	Bio-Rad	Myelin	142Nd	Our Lab	1:100
S100B	S100B/1706R	Novus	Astrocytes	167Er	Our Lab	1:400
TIM-3	D5D5R	Fluidigm	Co-inhibitory molecule	154Sm	Fluidigm	1:100
Vimentin	RV202	Fluidigm	Hypertrophic astrocytes	143Nd	Fluidigm	1:100